PHYSICAL REVIEW B **94**, 235209 (2016)

Oxygen vacancy related distortions in rutile TiO_2 nanoparticles: A combined experimental and theoretical study

G. C. Vásquez,[1,*] S. Zh. Karazhanov,[2] D. Maestre,[1] A. Cremades,[1] J. Piqueras,[1] and S. E. Foss[2]
[1]*Departamento de Física de Materiales, Facultad de CC. Físicas, Universidad Complutense, 28040, Madrid, Spain*
[2]*Institute for Energy technology, PO Box 40, 2027, Kjeller, Norway*

(Received 7 August 2016; revised manuscript received 22 October 2016; published 23 December 2016)

The effects of doubly ionized oxygen vacancies (${V_O}^{2+}$) on the electronic structure and charge distribution in rutile TiO_2 are studied by combining first-principles calculations based on density functional theory and experimental results from x-ray photoelectron and x-ray absorption measurements carried out in synchrotron facilities on rutile TiO_2 nanoparticles. The generalized gradient approximation of the Perdew-Burke-Ernzerhof functional has demonstrated its suitability for the analysis of the ${V_O}^{2+}$ defects in rutile TiO_2. It has been found that the presence of empty electronic states at the conduction band shifted ~1 eV from t_{2g} and e_g states can be associated with local distortions induced by ${V_O}^{2+}$ defects, in good agreement with Gauss-Lorentzian band deconvolution of experimental O K-edge spectra. The asymmetry of t_{2g} and e_g bands at the O-K edge has been associated with ${V_O}^{2+}$, which can enrich the understanding of studies where the presence of these defects plays a key role, as in the case of doped TiO_2.

DOI: 10.1103/PhysRevB.94.235209

I. INTRODUCTION

Titanium dioxide (TiO_2) has been the matter of interdisciplinary studies during the last few years because of its suitability for applications in photocatalysis, gas sensors, and optoelectronics. A large number of empirical and theoretical studies point out that many physical and chemical properties of TiO_2 mainly depend on structural defects, such as Ti interstitials, oxygen vacancies (V_O), and lattice disorder near the surface [1–6]. Therefore, understanding the effects related to structural defects in TiO_2 as well as developing appropriate methods for their identification are issues of technological interest.

Synchrotron radiation techniques as x-ray photoelectron spectroscopy (XPS), resonant XPS, and x-ray absorption spectroscopy (XAS) can provide information of the occupied states at the valence band (VB) and empty states at the conduction band (CB) [7], respectively, by an appropriate choice of the spectral region during the experiments. Occupied Ti($3d$) states near the Fermi level (E_F) can be detected by XPS on TiO_2 as a consequence of oxygen deficiency; however, the effects of structural defects on the CB have been less explored. The XAS O K-edge corresponds to electronic transitions from O($1s$) to empty O($2p$) states [7]. Even though the VB of TiO_2 is dominated mainly by O($2p$) states, the high hybridization degree with Ti($3d$) orbitals allows electron transitions from O($2p$) to Ti($3d$) states leaving partially empty O($2p$) states at the CB [8]. For this reason, the analysis of the absorption O K-edge is a useful experimental technique to scan the empty states at the CB for semiconductor oxides such as TiO_2. Actually, the O K-edge is commonly used as a fingerprint to identify the different TiO_2 polymorphs. The presence of structural defects, among other effects, can induce modifications in the XAS spectral shape, which should be considered in the spectral analysis.

Theoretical studies have been performed in order to reproduce the density of states (DOS) at the VB and the CB [9] using the density functional theory (DFT) approach, with good results for semiconducting oxides, such as TiO_2 [10]. In these studies, the presence of defects related to oxygen deficiency has to be considered. Neutral, single ionized, and double ionized oxygen vacancies, as well as titanium interstitials and some other oxygen-related defects, are usually considered in the rutile TiO_2 defect structure [6,11]. Among them, in our case, formation of oxygen vacancies is energetically favored as compared with formation of Ti interstitials [5,6], regarding that the nanoparticles under study were synthesized at low temperatures and under oxygen-rich conditions [12]. Oxygen vacancy formation in bulk rutile [12] as well as in all reduced surfaces [13] of rutile TiO_2 results in two electrons which tend to occupy $3d$ orbitals on neighboring Ti atoms leading to the generation of Ti^{3+} atoms. Therefore, the TiO_2 nanoparticles studied here are characterized by nonstoichiometry, which is associated with multiple bandgap defect-related states mainly due to the formation of oxygen vacancies and the subsequent generation of Ti^{3+} cations. Defect states near E_F related to neutral V_O have been simulated by other authors using DFT [14–16], which enabled us to explain the n-type behavior of TiO_2 [14,17]. The effects of V_O at the CB and the correlation with experimental data have been usually studied for highly oxygen-defective samples [18], for which the presence of oxygen vacancies is significantly higher than in conventional samples. However, oxygen vacancies are native defects in TiO_2, and less has been done on the correlation between calculations and experimental results on as-grown samples under standard conditions, for which oxygen vacancies are also common defects. In this paper, we focus on the theoretical and experimental analysis of the local-distortions at the O K-edge related to the presence of the energetically favored ${V_O}^{2+}$ defects [6].

Hence, we correlate the theoretical CB of rutile TiO_2, calculated by DFT, with experimental O K-edge measured by XAS at a synchrotron line from single phase rutile TiO_2 nanoparticles. Recent papers [19–22] aim to correlate

---

[*] gc.vasquez@ucm.es

O K-edge with structural defects in nanosized TiO_2 in order to explain their electronic, magnetic, and photocatalytic properties, but a correlation with theoretical approach, as included in this paper, was still needed. These nanoparticles have been previously analyzed by different techniques, such as transmission electron microscopy (TEM), cathodoluminescence (CL), and XPS [23], which will help to optimize the parameters used in our calculations. The correlation of theoretical and experimental observations results in a better understanding of the experimental data and sheds light on the analysis of the O K-edge and the effects related to oxygen vacancy related structural defects in rutile TiO_2. Moreover, these results can be also used as model for doped TiO_2 and other rutilelike semiconducting oxides.

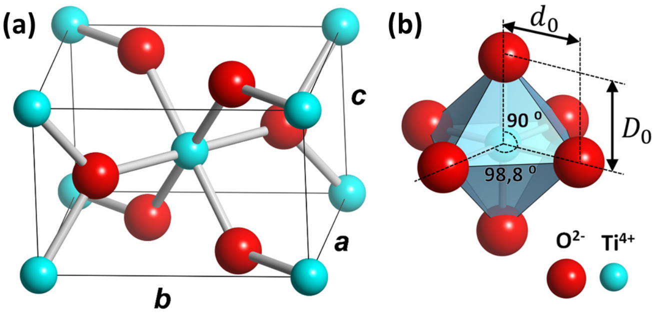

FIG. 1. Ball and stick models of (a) rutile TiO_2 unit cell and (b) single TiO_6 octahedron.

II. MATERIALS AND METHODS

Here, TiO_2 nanoparticles have been synthesized by a modified Pechini method [24] as reported in Ref. [23]. The nanoparticles present an average particle size of 20 nm, as deduced by the Scherrer formula after Rietveld analysis of the monochromatic x-ray data and TEM measurements (not shown here). The nanoparticle powder, pressed into pellets, was studied by XPS and XAS in total electron yield (TEY) mode at the BACH beamline of the Elettra synchrotron facility in Trieste. Before the XPS and XAS measurements, the samples were pre-evacuated to 10^{-6} Torr and heated under vacuum ($\sim$390 K) for a few hours before being transferred into the main chamber. A photon energy in the range of 450–457 eV and a total energy resolution of 200 meV were used during the acquisition of the photoemission spectra in normal incidence geometry. The XAS and XPS geometries employed for the acquisition of the experimental data involve penetration depths around 10 nm [25], the average dimensions of the nanoparticles under study being around 20 nm. Therefore, in this paper, we consider not only the last surface monolayers ($\sim$Å), but also the subsurface and core region of the nanoparticles ($\sim$nm). Hence, predominant bulk-related effects should be considered in the analysis of the XAS and XPS results acquired on the nanoparticles. Surface contributions to the XAS or XPS signals cannot be ruled out, although their intensity should be significantly smaller than the core related signals. The XAS spectra were fitted using Gaussian-Lorentzian peak shapes. The binding energy values were referenced to the C ($1s$) peak at 284.6 eV.

All the calculations in this paper were performed using the DFT implemented in the Vienna *Ab initio* Simulation Package (VASP) [26–28] together with the potential projector augmented-wave (PAW) method [29–31]. The core and valence electronic states were expanded with a plane-wave basis set. An energy cutoff of 500 eV was found optimal for our calculations. Standard PAW Perdew-Burke-Ernzerhof (PBE) pseudopotentials were employed to describe the Ti($3s3p3d4s$) and O($2s2p$) valence states. The computations have been performed within the PBE [32] generalized gradient approximation (GGA) exchange correlation functional as well as the Heyd-Scuseria-Ernzerhof (HSE; HSE06) hybrid functional containing a modified portion of the Fock exchange. Hybrid functionals as proposed by HSE [33,34] were performed in order to compare with PAW-PBE calculations for bulk rutile TiO_2 in order to ensure a good assessment of the study. In the hybrid functional, a standard value of the (short-range) Hartree-Fock exchange (25%) is mixed with a portion of PBE exchange (75%). In this paper, the screening parameter of 0.2 Å^{-1} is used as suggested by the HSE06 hybrid functional [33].

The defect calculations were performed using a $2 \times 2 \times 4$ (96 atoms) supercell for the doubly ionized oxygen vacancy ($V_O{}^{2+}$) using a $4 \times 4 \times 6$ mesh for the k-point sampling centered at the Γ point. A larger supercell, $3 \times 3 \times 5$ (270 atoms) including one oxygen vacancy, has been also considered for the calculations. However, as no significant changes were observed in the DOS as a function of the supercell size, in this paper, the calculations were carried out using a 96 atom supercell. The structural optimization for point defects in the supercell were performed starting from a preconverged unit cell and allowing ionic relaxation with energy convergence of 10^{-7} eV per atom and minimizing the forces on all atoms to less than 10^{-2} eV $\cdot$ Å^{-1}. The calculation of the Bader effective charges were performed using the Henkelman's grid-based algorithm for the Bader electron decomposition method [35]. The effective charges are defined as $Q_X = Z_X - q_{\text{Bader},X}$(X = Ti, O), where Z_X is the number of valence electrons and $q_{\text{Bader},X}$ is the calculated Bader charge for the corresponding X atom. Graphical illustrations depicted in the Figs. 1, 2, and 6 were plotted using the software VESTA [36].

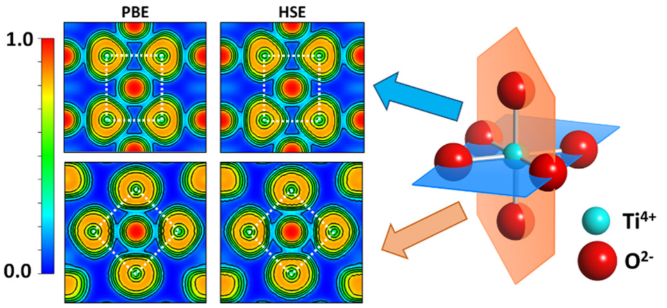

FIG. 2. Basal cross section (top) and apical cross section (bottom) of the ELF through a single octahedron. The octahedra contours are depicted in white dotted squares.

TABLE I. List of lattice parameters, bond length, energy band gap, and Bader effective charge calculated for the rutile. Comparison to experimental data and other theoretical studies is included.

	a (Å)	c (Å)	d_0(Å)	D_0(Å)	E_g(eV)	$Q_{Ti}(\|e\|)$	$Q_O(\|e\|)$
PBE	4.6534	2.9730	1.9642	2.0066	1.8	+2.23	−1.12
HSE06	4.5904	2.9541	1.9450	1.9805	3.2	+2.43	−1.21
Experiment[a]	4.5937	2.9587	1.946	1.984	3.0–3.1		
PBE[b]	4.650	2.971		2.006	1.77	+2.22	−1.12
HSE[b]	4.590	2.947		1.980	3.05		
LDA[b]	4.557	2.929			1.79		

[a] References [2,4,10,38].

[b] References [3,14,16].

III. RESULTS AND DISCUSSION

The rutile phase of TiO_2 consists of an infinite octahedral chain where each Ti^{4+} ion is surrounded by six O^{2-} ions. The point group symmetry of TiO_6 octahedron is reduced to D_{2h} because of the tetragonal and trigonal distortions. Figures 1(a) and 1(b) represent the tetragonal unit cell of the rutile phase of TiO_2 and a single TiO_6 octahedron, respectively. Short (d_0) and long (D_0) Ti-O bonds are indicated in Fig. 1(b). Table I summarizes the lattice parameters a and c, the short and long Ti-O bond lengths in the TiO_6 octahedron, the energy band gap (E_g) at the Γ point, and the Bader effective charge associated with Ti and O atoms, calculated using both PBE and HSE06 functionals. Results obtained by both PBE and HSE06 methods have been compared and evaluated in order to check the viability of these computational methods in the study of the high energy region of the CB as well as in the estimation of rutile TiO_2 structural parameters. The electronic structure and the analysis of the covalency degree of rutile TiO_2 has been studied by means of the DOS, partial DOS (pDOS), the Bader effective charge analysis, and the electron localization function (ELF) to visualize the charge density [37]. These results will be the basis of the study for the local and long-range effect for point defects such as the oxygen vacancy.

The results show that the lattice parameters and Ti-O bond lengths are in good agreement with experimental values, those calculated by PBE differ from experimental values around 1.3–0.5%, whereas the relative difference is around 0.15–0.05% for HSE06. The calculated effective charges for Ti and O atoms are 8% higher for the HSE06 approximation. However, both approximations indicate a slight covalent bonding since the Ti Bader effective charge is +2.23 |e| for PBE and +2.43 |e| for HSE06. This indicates that Ti is sharing a net charge of +1.77 |e| (PBE) and +1.57 |e| (HSE06) with the surrounding O atoms, considering that the expected oxidation state is Ti^{4+} in stoichiometric TiO_2. The calculated net shared charge or deviations from the O^{2-} oxidation state for O atoms are −0.88 |e| (PBE) and −0.79 |e| (HSE06). Therefore, the effective shared charge in each Ti-O bond can be determined dividing the net shared charge by the corresponding coordination number (six for Ti and three for O) giving as results 0.29 |e| and 0.26 |e| for PBE and HSE06, respectively, which shows that the hybrid functional predicts a higher ionic character than PBE. However, no significant differences are observed in the ELF obtained from computations using the PBE and HSE06 approximations, as observed in Fig. 2.

Figure 2 shows the ELF section for two different symmetry planes (basal and apical sections) in a single TiO_6 rutile octahedron, which are representative for the bulk crystal. A single octahedron contour has been depicted with white dotted squares with the Ti atom at the center and O atoms at the corners. In the basal plane, the titanium is coordinated with four oxygen atoms with constant Ti-O bond length (d_0) where the O-Ti-O angles formed are 81.2° and 98.8°, which is characteristic of a trigonal distortion. This plane belongs to the $\{110\}$ family planes, and each oxygen atom is coordinated with three different titanium atoms. In the apical section plane, the apical Ti-O bonds (D_0) are larger than the basal bonds, and the O-Ti-O angle is 90°, characteristic of the tetragonal distortion of the TiO_6 octahedra in rutile TiO_2. The slight covalent character of the Ti-O bonding is well observed since the ELF in the region between Ti and O atoms is nonzero, showing a small probability of finding electrons located in this region. However, the ELF value between Ti-O atoms is less than $0.15\mathrm{e}\cdot\mathrm{Å}^{-3}$ for both PBE and HSE approximations, which means a predominant ionic character in the Ti-O bonding [39].

The results of the calculations using PBE and HSE06 are in good agreement with each other except for the estimation of E_g. The calculated E_g using the PBE approximation is about 1.8 eV, far from the experimental value of 3.0–3.1 eV for rutile TiO_2. On the other hand, using HSE06, the calculated E_g is 3.2 eV, which shows a better agreement with experiments. However, Janotti *et al.* [14] reported that the band structure of the rutile phase is nearly equivalent for both approximations. The total electronic DOS and the pDOS for Ti($3d$) and O($2p$) states calculated for PBE and HSE06 functionals are represented in the Figs. 3(a) and 3(b), respectively, on which the E_F is set to zero. In both cases, the top of the VB is dominated by O($2p$) states, and the CB edge is dominated by empty Ti($3d$) states. The presence of O($2p$) and Ti($3d$) states in both VB and CB indicates a considerable hybridization degree of Ti-O bonds, resulting in a crystal field (CF) splitting of Ti($3d$) orbitals into the t_{2g} and e_g states [10] within the CB, that is characteristic of Ti ions in octahedral coordination symmetry [40,41]. Despite the E_g underestimation observed in PBE, the main characteristics of the total DOS and pDOS at the VB and CB are equivalent in both approximations, as for example the VB and CB width as well as the location of the t_{2g} and e_g states, which are characteristic of the rutile phase of TiO_2 [10,41,42].

Oxygen vacancy (V_O) is a common defect in TiO_2, as well as in other semiconducting oxides, the presence of which is

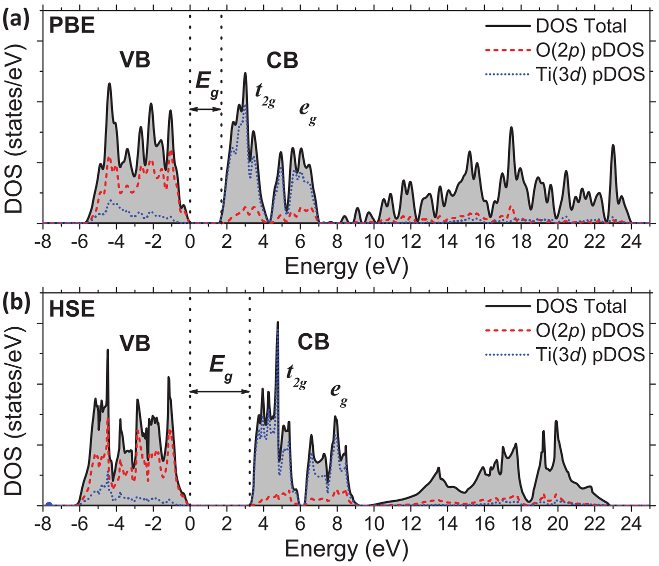

FIG. 3. Total DOS and O (2*p*) and Ti (3*d*) pDOS calculated for (a) the PBE functional, and (b) hybrid HSE functional. The Fermi level is set to zero.

related to most of the physical-chemical properties of the material; hence, it should be considered in the theoretical study and the analysis of experimental results [1]. The V_O defect can be simulated by removing one oxygen atom from the rutile lattice. Depending on the number of electrons, the charge of the V_O can be neutral ($V_O{}^0$) if two electrons occupy the vacancy site, +1 ($V_O{}^{1+}$) if there is only one electron, or +2 ($V_O{}^{2+}$) if the vacancy contains no electrons. As mentioned before, in TiO_2, each O atom is coordinated by three Ti atoms. Upon removing the central O atom, the three Ti(3*d*) dangling bonds tend to point to the V_O site. After ionic relaxation, the Ti(3*d*) states from the nearest Ti atoms are combined creating a symmetric defect state with a position, relative to the E_F, which depends on the electronic charge of the V_O [5,14,15]. As mentioned above, one of the limitations of the PBE functional is the underestimation of E_g that influences the V_O-derived intermediate band, which might come out either fully completed or just partially filled with electrons. Furthermore, the occupied defect state might overlap with the CB becoming unstable for this functional [14]. However, since the $V_O{}^{2+}$ defect is an empty state, it is allowed to overlap within the CB and can be stable using the PBE functional [14], overcoming the limitation of the bandgap underestimation. Furthermore, several DFT approximations such as HSE06 [6,14], local density approximation (LDA) + U [3], or GW [15] point out that the $V_O{}^{2+}$ is the most energetically stable oxygen vacancy in rutile TiO_2, and the calculated formation energy is almost the same as that calculated using PBE [14]. These previous papers show the suitability of the use of the PAW-PBE approximation for the study of $V_O{}^{2+}$ defects in TiO_2; therefore, this defect has been considered in the theoretical and experimental study described in this paper. Calculations obtained by both PBE and HSE06 are comparable, despite the underestimation of E_g by using PBE, but the former method involves reduced time of calculation. Hence, the PBE method has been hereinafter employed in the study of oxygen defects in rutile TiO_2.

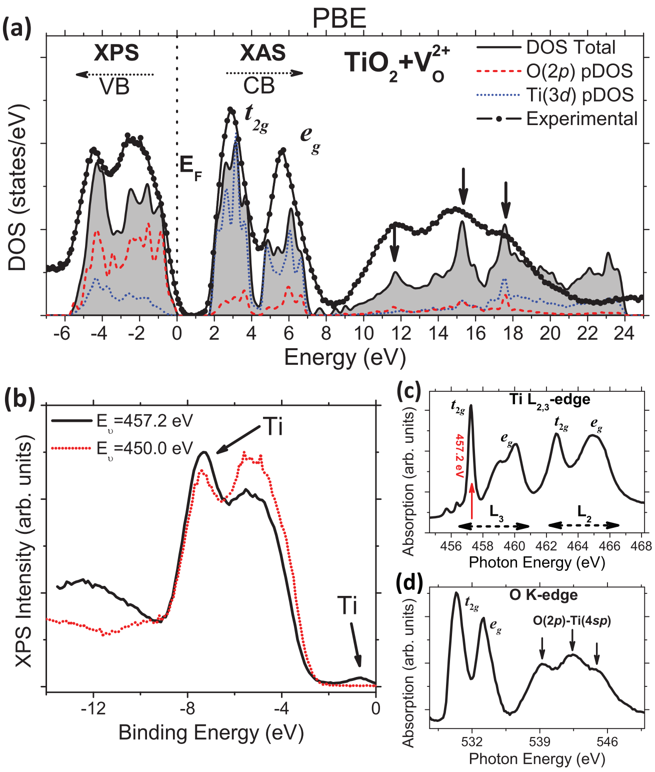

FIG. 4. (a) Calculated DOS for the $V_O{}^{2+}$ defect in the PBE approximation. Dotted lines indicate experimental data for XPS and XAS spectra. Experimental data from TiO_2-np: (b) Ti-resonant XPS spectrum and out-of-resonance XPS spectrum at the VB. (c) Ti $L_{2,3}$-edge spectrum, and (d) Absorption O K-edge. The peak marked in (c) is the photon energy applied in (b) for Ti-resonant photoemission experiment.

Figure 4(a) shows the calculated DOS and pDOS for O(2*p*) and Ti(3*d*) states corresponding to the $V_O{}^{2+}$ defect, where the E_F is set to zero. Experimental data from the XPS VB spectrum, acquired with a photon energy of 450 eV, and XAS O K-edge spectrum obtained from TiO_2 nanoparticles have been included for comparison with the theoretical DOS. The analysis shows that the DOS at the VB region presents similar characteristics to those of the XPS spectrum of the VB. In particular, according to the resonant XPS spectrum [Fig. 4(b)] obtained using the photon energy corresponding to the Ti $L_3(t_{2g})$ absorption peak at $E_\nu = 457.2$ eV in Fig. 4(c), the states located at 4–5 eV below E_F in the calculated DOS [Fig. 4(a)] correspond to contributions of hybridized Ti(3*d*)-O(2*p*) states at the VB. Defect states at about 0.8 eV below the E_F, related to occupied Ti(3*d*) orbitals, confirm the presence of oxygen defects in our samples [23,43,44]. Locations of the peaks corresponding to the e_g and t_{2g} states in CB, determined from DFT calculations, are in agreement with those established experimentally from the O K-edge spectrum. The energy difference of about 2.8 eV [41] between the absorption bands and the related empty states in the calculated CB agrees with the CF splitting for TiO_2. At higher energies, the O K-edge spectrum shows three peaks located at around 539, 542, and 545 eV [marked with arrows in Fig. 4(d)] attributed to O(2*p*)-Ti(4*s*) and O(2*p*)-Ti(3*pd*) hybridized states [10,42]. These three peaks are considered

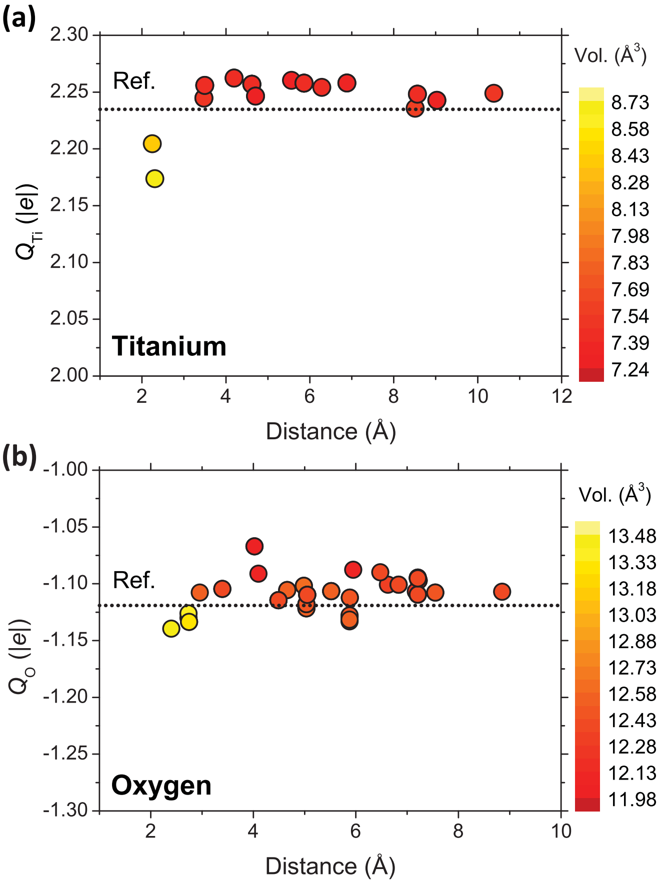

FIG. 5. Effective Bader charges as a function of the distance from the V_O^{2+} defect calculated for (a) Ti and (b) O atoms with respect to the bulk reference (dotted line). Color bar represents their corresponding Bader volume.

as a fingerprint of the rutile phase of TiO_2. In the calculated CB, they can be also clearly identified [Fig. 4(a), marked with arrows]. These results confirm the suitability of the PAW-PBE functional in the study of the V_O^{2+} defects in rutile TiO_2.

Figures 5(a) and 5(b) show the effective Bader charges calculated for Ti and O atoms, respectively, as a function of their absolute distance from the oxygen defect V_O^{2+}. Dotted lines represent the reference effective charges calculated for bulk TiO_2. The corresponding Bader volume of the atoms, defined as the volume enclosed by a surface of minimum charge density surrounding each atom, are represented by different colors with respect to the color bar at the right side of the Figs. 5(a) and 5(b). It can be noticed that V_O^{2+} mainly affects the effective charge in a range from 2 Å to approximately 7 Å, and the effective Bader charge progressively tends to reference values as the distance from defect increases (10–12 Å). Figure 5(a) shows that the Bader volume of the Ti atoms nearest to the defect V_O^{2+} (∼2 Å) increase, and their effective charge decreases. Taking into account that the presence of V_O breaks three Ti-O bonds from the nearest Ti atoms, the effective charge reduction could be due to charge redistribution by increasing the covalency with the bonded O atoms. In the case of O atoms, the Bader volume of the O atoms nearest to the V_O^{2+} increases, and the effective charge is slightly decreased with respect to the reference value, as shown in Fig. 5(b). Unlike previous analysis of Ti atoms, in this case, the nearest O atoms are still coordinated with three Ti atoms. So the effective charge and volume modifications could be the consequence of the effect of lattice distortions induced by the oxygen vacancy.

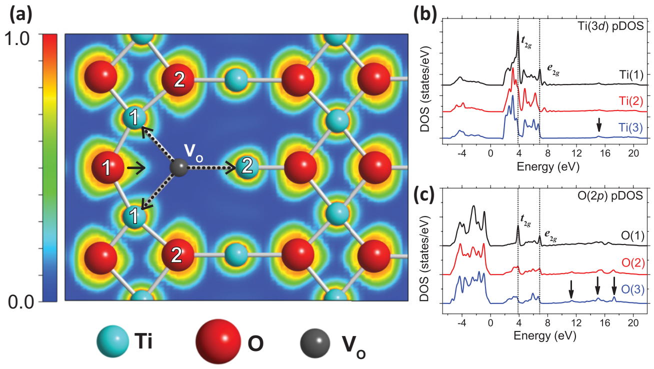

FIG. 6. (a) Ball and stick diagram corresponding to the (110) plane and the corresponding ELF cross-section for the V_O^{2+} defect. The nearest atoms from the V_O are labeled as (1) and (2). (b) Ti(3d), and (c) O(2p) pDOS from the atoms (1) and (2) and an atom far from the V_O, labeled as (3).

The electronic distortions induced by the V_O^{2+} in the relaxed supercell can be better appreciated in the ELF section corresponding to the (110) plane, represented in the Fig. 6(a). The electron density around the atoms close to the defect tends to occupy the empty sites; however, the displacements of Ti and O cores are opposite to each other as a consequence of a higher Coulombic repulsion between Ti^{4+} and V_O^{2+}. Here, Ti cores are displaced outward from the V_O, whereas O cores are slightly displaced towards the V_O as it can be appreciated in the ball and stick diagram of the Fig. 6(a). The dotted lines represent the broken bonds, and the arrows indicate the direction of Ti and O displacements, due to the geometric relaxation caused by the oxygen removal and formation of V_O^{2+}. Here, Ti(1) and Ti(2) displacements are $d_1 = 1.17 d_0$ and $D_2 = 1.12 D_0$, respectively, in relation to stoichiometric TiO_2 (see Table I).

Localization of V_O^{2+} states within the CB can be observed by analyzing the Ti(3d) pDOS and the O(2p) pDOS in the Figs. 6(b) and 6(c), respectively, of the atoms nearest to the V_O^{2+} (∼2 Å), labeled as (1) and (2) and atoms located far from the defect [not shown in Fig. 6(a)], at ∼7 − 10 Å from the vacancy, labeled as (3). Both Ti(1) and O(1) show localized states at around 4 and 7 eV above the E_F, marked with dotted lines [Figs. 6(b) and 6(c)], at higher energies as compared to the observed peak maxima at Ti(3) and O(3). The t_{2g} and e_g states from Ti(2) and O(2) atoms are also shifted, to a lesser extent, towards higher energies. This agrees with the observation of the Bader charge variations with respect to the bulk reference value and the induced lattice distortions. The calculated Ti(3d) and O(2p) pDOS indicate that the effect of V_O^{2+} is strong for atoms at ∼2 Å and vanishes for atoms at distances greater than ∼7 Å, which have electronic characteristics similar to bulk rutile.

Experimental XPS spectrum of undoped rutile TiO_2 nanoparticles (nps) reported in a previous paper [23] indicates high concentration of Ti^{3+} defects, due to oxygen deficiency, at the surface of the nanoparticles. The Ti^{3+} content was

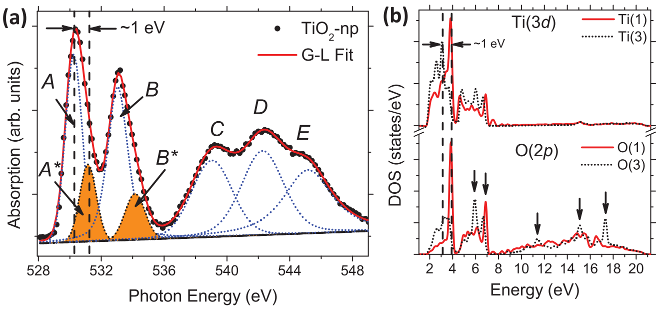

FIG. 7. (a) Deconvolution of the experimental absorption O K-edge into seven G-L bands. (b) Calculated Ti($3d$) and O($2p$) pDOS at the CB region where empty states from (1) are shifted with respect to (3).

estimated by Gaussian deconvolution of Ti($2p_{3/2}$) core XPS spectrum into the Ti^{3+} and Ti^{4+} bands. The ratio between these bands gives an approximation of the Ti^{3+} defect content in the samples that was related to oxygen deficiency in the TiO_2 samples [23]. In addition, according to Morgan and Watson [13], for all the reduced common rutile surfaces, the excess charge associated with the defect states is primarily localized on two Ti sites neighboring the vacancy, formally reducing these to Ti^{3+}. Similar to the results obtained for bulk calculation, the oxygen vacancy at the (110) and (100) surfaces, which are the ones with lower surface energies, gives rise to band gap states between 0.7 to 1.4 eV from the CB bottom, and therefore, some contribution of the surface vacancies to the present results cannot be ruled out, although due to the geometry of the experiments, a predominant bulk signal is expected, as explained in the experimental section.

Figure 7(a) represents the band deconvolution of the experimental O K-edge spectrum from rutile TiO_2 nps, shown in Fig. 4(d). In this case, the minimum number of Gauss-Lorentz (G-L) bands necessary to perform the deconvolution is seven. Two G-L bands for each t_{2g} and e_g state located between 528 and 536 eV, and three G-L bands for the complex hybridized region between 536 to 550 eV. These results are in agreement with the calculations performed in this paper considering the presence of the ${V_O}^{2+}$ defect in rutile TiO_2, as described above. In Fig. 7(a), it can be appreciated a dominant band (A) approximately at the center of the t_{2g} related band and a weaker absorption band shifted about 1 eV higher (A*). This trend is repeated for the e_g related bands (B and B*). Here, A* and B* G-L bands are shadowed in Fig. 7(a). The origin of the A* and B* bands observed in the O K-edge spectrum is not well known. Muller *et al.* [18] observed the local effect of V_O at the O K-edge from oxygen defective $SrTiO_{3-\delta}$ samples using the electron energy loss spectroscopy (EELS) technique, with a physical meaning equivalent to that of XAS. The effect was observed in high oxygen defective samples (with δ up to 0.25) accompanied by a Ti^{4+} reduction into Ti^{3+}. In the study of Ti_xO_y complexes reported by Yoshiya *et al.* [45], the location of the O K-edge varies as a function of the Ti oxidation state, being shifted to higher energies as the oxidation state is reduced. In that study, the energy shift for Ti_2O_3 with respect to TiO_2 is about 1 eV. Chen *et al.* [22] performed a Gaussian deconvolution to analyze the Ti L_3-edge from TiO_2 nanotubes. The modifications observed were assigned to variations in the concentration of oxygen defects. However, in their study, the O K-edge was not analyzed, despite that the spectra show similar features as those discussed in this paper. Thakur *et al.* [20] identified two features in the O K-edge located around ~1.2 eV at higher energies from the t_{2g} and e_g bands after heavy ion irradiation on TiO_2. They assigned the presence of these features to local distortions induced by irradiation [21], but no theoretical support or references were provided. In a recent paper by Tian *et al.* [19], a linear least-square fitting method was performed to quantify the Ti_2O_3/TiO_2 ratio on the surface of TiO_2 nanoparticles using O K-edge spectra acquired using the EELS technique. Despite that they achieve the fitting with relatively high accuracy, the residuals from the fitted and experimental measurement still show two features that match with our A* and B* bands (see Figs. 2(b) and 2(c) of Ref. [19]).

In this paper, theoretical calculations have been performed in order to shed light on the origin of these A* and B* bands. Figure 7(b) shows the calculated pDOS for the nearest O(1) and Ti(1) atoms together with the O(3) and Ti(3) atoms far from the ${V_O}^{2+}$ defect, also depicted in the Figs. 6(b) and 6(c). In both cases, the defect states at the CB are clearly shifted about 1 eV toward higher energies, which can be assigned to the A* and B* bands obtained by deconvolution of the experimental O K-edge [(Fig. 7(a)]. In this manner, the presence of the A* bands could not be assigned only to coordinated Ti^{3+}, as deduced from other studies [18,45,46], because in those cases, the CF splitting of Ti could be also reduced [46]; hence, according to our theoretical and experimental results, A* and B* bands can be assigned to the presence of local distortions induced by ${V_O}^{2+}$ defects whose empty electronic states, overlapped with the CB, are blueshifted approximately 1 eV with respect to that from the undistorted lattice. The relation of these A* and B* bands with the presence of ${V_O}^{2+}$ defects in rutile TiO_2 could lead to enrich the analysis of the O K-edge and, therefore, shed light into the identification of these defects and the understanding of the oxygen deficiency related phenomena.

Therefore, special attention should be paid in the analysis of the XAS signal, in particular to the O K-edge, as relevant information of the structure of defect and the effects caused by doping can be also achieved.

IV. CONCLUSIONS

First-principles calculations based on DFT were performed in this paper to study the local effect of ${V_O}^{2+}$ defects in rutile TiO_2 by analyzing the Bader effective charge, ELF, and DOS. The results show that the presence of oxygen vacancy generates local distortions and the creation of empty electronic states at the CB showing narrow features with maxima shifted ~1 eV from the t_{2g} and e_g states in bulk TiO_2. Experimental XPS and XAS measurements from single-phase rutile TiO_2 nanoparticles have been used to study the VB and CB, respectively, showing good agreement with the calculated DOS. Calculated Ti($3d$) pDOS and O($2p$) pDOS reproduce all the features of the CB that are characteristic of the rutile phase of TiO_2 as compared to the experimental O K-edge, and the PBE functional has demonstrated its suitability in the analysis of ${V_O}^{2+}$ defects. The G-L band deconvolution of the O K-edge shows the presence of additional bands within the t_{2g} and e_g related bands, named as A* and B*, that are also shifted 1 eV towards higher energies, in agreement with our calculations. These A* and B* bands have been associated with the presence of $V_O{}^{2+}$ defects in rutile TiO_2, which should be considered in further research, as an example in the study of doped rutile TiO_2. By combining computational and experimental results, relevant information of the structure of defects on the CB can be achieved by the exhaustive analysis of the O K-edge, which can be a valuable tool for a deeper understanding of the effects of dopants in the defect structure.

ACKNOWLEDGMENTS

This paper has been supported by the Norway, Iceland, Liechtenstein Science and Sustainability (NILS)/EEA Grants "Sustainable oxide materials and nanostructures for energy related applications (SUSOX)" (Project No. 008-ABELCM-2013), Norwegian Metacenter for Computational Science (Notur) Project No. nn4608k, Ministry of Economy, Industry and Competitiveness (MINECO)/European Regional Development Fund (FEDER) Project No. MAT2015-65274-R, and Consolider Ingenio Project No. CSD 2009-00013. The authors thank Dr. A. Pishtshev for practical help, Dr. J. Ramírez-Castellanos for kindly providing the TiO_2 nanoparticles, and the BACH beamline staff for useful advice on XPS and XAS measurements at the Elettra Synchrotron in Trieste. The work by S.Z.K. has been supported by New Indigo Project No. 237643/E20.

---

[1] X. Chen and Samuel S. Mao, Chem. Rev. **107**, 2891 (2007).
[2] J. P. Crocombette and F. Jollet, J. Phys. Condens. Matter **6**, 10811 (1994).
[3] S.-G. Park, B. Magyari-Köpe, and Y. Nishi, Phys. Rev. B **82**, 115109 (2010).
[4] U. Diebold, Surf. Sci. Rep. **48**, 53 (2003).
[5] A. Boonchun, P. Reunchan, and N. Umezawa, Phys. Chem. Chem. Phys. **18**, 30040 (2016).
[6] P. Deák, B. Aradi, and T. Frauenheim, Phys. Rev. B **92**, 045204 (2015).
[7] G. Lucovsky, J. G. Hong, C. C. Fulton, N. A. Stoute, Y. Zou, R. J. Nemanich, D. E. Aspnes, H. Ade, and D. G. Schlom, Microelectron. Reliab. **45**, 827 (2005).
[8] F. M. F. de Groot, M. Grioni, J. C. Fuggle, J. Ghijsen, G. A. Sawatzky, and H. Petersen, Phys. Rev. B **40**, 5715 (1989).
[9] N. Jiang and J. C. H. Spence, Phys. Rev. B **70**, 245117 (2004).
[10] B. Jiang, J. M. Zuo, N. Jiang, M. O'Keeffe, and J. C. H. Spence, Acta Crystallogr., Sect. A: Found. Crystallogr. **59**, 341 (2003).
[11] M. K. Nowotny, L. R. Sheppard, T. Bak, and J. Nowotny, J. Phys. Chem. C **112**, 5275 (2008).
[12] B. J. Morgan and G. W. Watson, J. Phys. Chem. C **114**, 2321 (2010).
[13] B. J. Morgan and G. W. Watson, J. Phys. Chem. C **113**, 7322 (2009).
[14] A. Janotti, J. B. Varley, P. Rinke, N. Umezawa, G. Kresse, and C. G. Van de Walle, Phys. Rev. B **81**, 085212 (2010).
[15] A. Malashevich, M. Jain, and S. G. Louie, Phys. Rev. B **89**, 075205 (2014).
[16] J. Stausholm-Møller, H. H. Kristoffersen, B. Hinnemann, G. K. H. Madsen, and B. Hammer, J. Chem. Phys. **133**, 144708 (2010).
[17] D. C. Cronemeyer, Phys. Rev. **113**, 1222 (1959).
[18] D. A. Muller, N. Nakagawa, A. Ohtomo, J. L. Grazul, and H. Y. Hwang, Nature **430**, 657 (2004).
[19] M. Tian, M. Mahjouri-Samani, G. Eres, R. Sachan, M. Yoon, M. F. Chisholm, K. Wang, A. A. Puretzky, C. M. Rouleau, D. B. Geohegan, and G. Duscher, ACS Nano **9**, 10482 (2015).
[20] H. Thakur, P. Thakur, R. Kumar, N. B. Brookes, K. K. Sharma, A. P. Singh, Y. Kumar, S. Gautam, and K. H. Chae, Appl. Phys. Lett. **98**, 192512 (2011).
[21] H. Thakur, R. Kumar, P. Thakur, N. B. Brookes, K. K. Sharma, A. Pratap Singh, Y. Kumar, S. Gautam, and K. H. Chae, J. Appl. Phys. **110**, 83718 (2011).
[22] C. L. Chen, C.-L. Dong, C.-H. Chen, J.-W. Wu, Y.-R. Lu, C.-J. Lin, S. Ya Hsuan Liou, C.-M. Tseng, K. Kumar, D.-H. Wei, J. Guo, W.-C. Chou, and M.-K. Wu, Phys. Chem. Chem. Phys. **17**, 22064 (2015).
[23] G. C. Vásquez, M. A. Peche-Herrero, D. Maestre, A. Cremades, J. Ramírez-Castellanos, J. M. González-Calbet, and J. Piqueras, J. Phys. Chem. C **117**, 1941 (2013).
[24] M. Pechini, US Patent No. 3330697 (1967).
[25] F. de Groot and A. Kotani, *Core Level Spectroscopy of Solids* (CRC Press, Boca Raton, Florida, 2008).
[26] G. Kresse and J. Furthmüller, Phys. Rev. B **54**, 11169 (1996).
[27] G. Kresse and J. Furthmüller, Comput. Mater. Sci. **6**, 15 (1996).
[28] G. Kresse and J. Hafner, Phys. Rev. B **49**, 14251 (1994).
[29] G. Kresse and D. Joubert, Phys. Rev. B **59**, 1758 (1999).
[30] G. Kresse and J. Hafner, Phys. Rev. B **47**, 558 (1993).
[31] P. E. Blöchl, Phys. Rev. B **50**, 17953 (1994).
[32] J. P. Perdew, K. Burke, and M. Ernzerhof, Phys. Rev. Lett. **77**, 3865 (1996).
[33] A. V. Krukau, O. A. Vydrov, A. F. Izmaylov, and G. E. Scuseria, J. Chem. Phys. **125**, 224106 (2006).
[34] J. Heyd, G. E. Scuseria, and M. Ernzerhof, J. Chem. Phys. **118**, 8207 (2003).
[35] W. Tang, E. Sanville, and G. Henkelman, J. Phys. Condens. Matter **21**, 84204 (2009).
[36] K. Momma and F. Izumi, J. Appl. Crystallogr. **44**, 1272 (2011).
[37] A. D. Becke and K. E. Edgecombe, J. Chem. Phys. **92**, 5397 (1990).
[38] A. Amtout and R. Leonelli, Phys. Rev. B **51**, 6842 (1995).
[39] B. Silvi and A. Savin, Nature **371**, 683 (1994).
[40] F. M. F. de Groot, M. O. Figueiredo, M. J. Basto, M. Abbate, H. Petersen, and J. C. Fuggle, Phys. Chem. Miner. **19**, 140 (1992).
[41] F. M. F. De Groot, J. Faber, J. J. M. Michiels, M. T. Czyyk, M. Abbate, and J. C. Fuggle, Phys. Rev. B **48**, 2074 (1993).
[42] S. O. Kucheyev, T. van Buuren, T. F. Baumann, J. H. Satcher, T. M. Willey, R. W. Meulenberg, T. E. Felter, J. F. Poco, S. A. Gammon, and L. J. Terminello, Phys. Rev. B **69**, 245102 (2004).
[43] G. Drera, L. Sangaletti, F. Bondino, M. Malvestuto, L. Malavasi, Y. Diaz-Fernandez, S. Dash, M. C. Mozzati, and P. Galinetto, J. Phys. Condens. Matter **25**, 75502 (2013).
[44] Y. Wang, H. Sun, S. Tan, H. Feng, Z. Cheng, J. Zhao, A. Zhao, B. Wang, Y. Luo, J. Yang, and J. G. Hou, Nat. Commun. **4**, 2214 (2013).
[45] M. Yoshiya, I. Tanaka, K. Kaneko, and H. Adachi, J. Phys. Condens. Matter **11**, 3217 (1999).
[46] E. Stoyanov, F. Langenhorst, and G. Steinle-Neumann, Am. Mineral. **92**, 577 (2007).